Journal of the European Ceramic Society 38 (2018) 4906–4914

Contents lists available at ScienceDirect

Journal of the European Ceramic Society

journal homepage: www.elsevier.com/locate/jeurceramsoc

Original Article

Flash pyrolysis of polymer-derived SiOC ceramics

Ruixin Ma[a], Donald Erb[b], Kathy Lu[b,*]

[a] Department of Environmental Engineering, North China Institute of Science and Technology, Beijing 101601, China
[b] Department of Materials Science and Engineering, Virginia Tech, Blacksburg, VA 24061, USA

ARTICLE INFO

Keywords:
SiOC
Flash pyrolysis
Microstructure
Phase separation
Nucleation

ABSTRACT

For the first time, flash pyrolysis was carried out to fabricate polymer derived silicon oxycarbide (SiOC) ceramics. With the application of a DC electric field at a furnace temperature of only 780 °C, the SiOC ceramics exhibit characteristics that usually have to be pyrolyzed at ~1300 °C. Both electric field and current density accelerate the SiOC microstructure development, causing carbon and SiC phases to form at > 520 °C lower pyrolysis temperatures than conventional within the SiOC matrix. With higher electric fields, the samples experience greater mass loss and linear shrinkage, while also forming more SiC and a more ordered carbon phase. The SiC formation inversely impacts the carbon content, causing a decrease in electrical conductivity. Further, reducing current density results in significant carbon precipitation without SiC formation. The fundamentals can be explained based on increased nucleation rate by the electrical field, accompanied by Joule heating and electromigration. This work is the first to demonstrate the great potential of flash pyrolysis on accelerated phase separation of polymer derived SiOC.

1. Introduction

Silicon oxycarbide (SiOC) is a polymer derived ceramic that has gained an increasing interest due to a wide variety of advantages such as thermal stability, chemical and oxidation resistance, tunable nano- and/or micro-structures, relatively low processing temperatures, and functional properties [1–3]. Pyrolysis is an important step in the fabrication of polymer-derived SiOC, and pyrolysis temperature dictates the microstructure of the ceramic [4]. Upon pyrolysis to temperatures greater than 1100 °C, the SiOC matrix evolves into nano-sized SiO_2 domains and a disordered graphitic phase embedded in an amorphous SiOC matrix [5–7]; at pyrolysis temperatures greater than 1300 °C, the SiOC matrix further phase separates, forming SiC nanocrystals and additional amorphous SiO_2 and graphitic domains [2,3,8]. Depending on the microstructure, the properties of the SiOC ceramic, such as electrical conductivity and oxidation resistance, can be greatly altered [9–11].

Traditionally, SiOC is fabricated simply by pyrolysis in an inert atmosphere. However, other techniques have been used to synthesize SiOC in the presence of external fields, including microwave assisted pyrolysis [12], spark plasma sintering (SPS) [13,14], and field assisted sintering (FAST) [15–17]. For microwave assisted pyrolysis, the graphitic phase is more stable at higher temperatures and less SiC is formed compared to conventional pyrolysis [12]. For SPS, several studies have found increased growth and ordering of the carbon phase, which have also been reported during fabrication of SiC using SPS [18]. As a result, the SiOC and SiC samples fabricated using SPS have higher electrical conductivity compared to traditional pyrolysis [13,18]. For FAST, the microstructure of the pyrolyzed SiOC is no different compared to traditional heating at 1400 °C, but the carbothermal reduction of the SiO_2 domains into SiC can be suppressed up to 1600 °C [15].

A new field-assisted technique, flash sintering, was reported in 2010 [19]. It can densify samples in short periods of time (as fast as 5 s) and, most importantly, at furnace temperatures significantly lower than those in conventional sintering [19]. During the flash event, the conductivity of the samples experiences a sharp nonlinear increase, accompanied by a sharp increase in the densification of the sample. The sharp conductivity increase leads to significant Joule heating, which can heat the sample several hundred degrees Celsius higher than the furnace temperature. Flash sintering was first reported for yttrium-stabilized zirconia [19] and was later successfully demonstrated in many ceramic materials, such as magnesia-doped alumina, strontium titanate, cobalt manganese oxide, and gadolinium-doped barium cerate [19–25]. However, flash pyrolysis of polymer derived ceramic materials such as SiOC has not yet been reported. Given that the starting polymer precursors are insulating and the resulting SiOC microstructure contains a conductive carbon phase, it should allow for the flash and Joule heating to occur. Further, carbon with an applied electric field can

* Corresponding author at: 213 Holden Hall, Virginia Tech, Blacksburg, VA 24061, USA.
E-mail address: klu@vt.edu (K. Lu).

https://doi.org/10.1016/j.jeurceramsoc.2018.07.010
Received 18 June 2018; Received in revised form 2 July 2018; Accepted 8 July 2018
Available online 10 July 2018
0955-2219/ © 2018 Elsevier Ltd. All rights reserved.

undergo ordering due to electromigration, or the collision of electrons/holes and defects, which may cause further changes within the SiOC microstructure [26].

In this study, flash pyrolysis of SiOC was investigated for the first time. The effects of flash conditions were examined. The corresponding thermophysical changes, SiOC phase separation, microstructure, and electrical properties were studied. The phase evolution driving force difference with and without the electrical field was analyzed for the first time, which can be successfully used to explain the accelerated phase evolution.

2. Materials and methods

2.1. Material preparation

Commercially available polysiloxane (PSO, $[-Si(C_6H_5)_2O-]_3[-Si(CH_3)(H)O-]_2[-Si(CH_3)(CH=CH_2)O-]_2$, SPR-684, Gelest Inc., Schenectady, NY) was chosen as the base precursor and 2.1–2.4% platinum-divinyltetramethyldisiloxane complex in xylene (Pt catalyst, Gelest Inc., Morrisville, PA) was used as the catalyst. Solutions with PSO and 10 vol% acetone as a solvent, relative to the PSO volume, were sonicated for 10 min and then mixed in a high energy mill (SPEX 8000 M Mixer/Mill, SPEX SamplePrep, Metuchen, NJ) for 10 min to form a homogeneous mixture. Next, the Pt catalyst (1 wt% relative to PSO) was added, the mixtures were mixed again in a high energy ball mill for 5 min, and then poured into aluminum foil molds. The mixtures were placed into a vacuum chamber and vacuumed for 10 min at 200 Torr to remove any solvents and bubbles in the solutions. The molds were then placed in an oven to crosslink at 50 °C for 12 h and then at 120 °C for 6 h to obtain preceramic green bodies.

2.2. Flash pyrolysis

Flash pyrolysis was achieved using the apparatus shown in Fig. 1. A green body was cut and polished into cylindrical shapes roughly 10 mm in diameter and 3 mm in thickness. A silver-palladium paste (conductor type 9627, ESL Electro Science, King of Prussia, PA) was applied to the sample and dried in order to achieve good electrical contact (minimizing contact resistance) and serve as the electrodes. The sample was then placed into a zirconia crucible. The electrical connections of the electrodes to the power supply were made by Pt wires.

The sample was put into a tube furnace (1730-20 Horizontal Tube Furnace, CM Furnaces Inc., Bloomfield, NJ) and pyrolyzed in argon with a flow rate of about 70 std $cm^3\ s^{-1}$ and a heating rate of 5 °C min^{-1} to 300 °C. The furnace was then heated up to 780 °C at 2 °C min^{-1}. At this point, an electric field was applied. Two commercial DC power sources (Bertan 210-01R Spellman, Hauppauge, NY and FB200 Fisher Scientific) were used to apply a specific voltage to the specimen up to a limiting current, at which the power supply automatically switched to the current control mode. The limiting current was either 0.4 A or 2 A. The power supply was shut off shortly after the flash occurred. An additional sample was pyrolyzed to 1300 °C without an applied electric field with the same heating procedure to serve as a comparison.

The samples were labelled as T-X-Y, where T is the pyrolysis temperature (780 °C or 1300 °C), X is the electric field applied to the sample (0, 30, 40, or 50 V mm^{-1}), and Y is the current limit set on the power supply (0.4 or 2 A). The ceramic yield and linear shrinkage of the samples were calculated using the mass and dimensions of the samples before and after pyrolysis. The phase compositions of the pyrolyzed samples were analyzed in an X'Pert PRO diffractometer (PANalytical B.V., EA Almelo, the Netherlands) with Cu Kα radiation. Raman spectra were recorded on a Horiba spectrometer (JY Horiba HR 800) with an excitation wavelength of 514 nm produced by an Ar laser between the spectral range of 100–4000 cm^{-1}. The microstructures of the pyrolyzed ceramics were studied using a transmission electron microscope (JEOL 2100, JEOL USA, Peabody, MA); the samples were prepared by grinding in a mortar and then dispersing in absolute ethanol. The electrical conductivity of the samples was measured in air at room temperature in a four-point probe configuration using a potentiostat (VersaSTAT 3, Princeton Applied Research, Oak Ridge, TN).

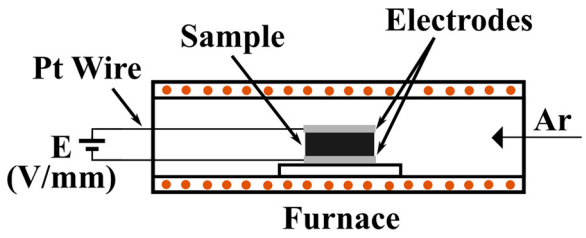

Fig. 1. Schematic representation of the flash pyrolysis apparatus.

3. Results and discussion

3.1. Flash pyrolysis

Consistent with the signature behavior of flash sintering, for the SiOC sample pyrolysis, there is a rapid power density increase as the specimen becomes electrically conductive due to the combined impact from the applied electric field and heating, which end when the power supply changes from the voltage control mode to the current control mode. The volumetric power density W_V, current density J, and electrical field strength E obey the well-known relation:

$$W_V = J \cdot E \tag{1}$$

After an incubation time of 18–28 min, the current density suddenly increases and the applied field decreases. This change corresponds to a significant increase in the conductivity of the samples due to the precipitation of carbon from the SiOC matrix (as seen in Section 3.3), forming a conductive network. As the current approaches the limit of the power supply, 2 A (maximum current density), the electric field slightly increases again. The current continuously increases during the slight electric field increase, so the conductivity of the samples also continuously increases during the entire process even though it is slower than that at the beginning of the flash. This can be explained by more SiC formation and consumption of the C phase, to be discussed in Section 3.3. The sudden power density increase, current density increase, and electric field decrease over time are shown in Fig. 2. The zero point of the time scale refers to the beginning of the application of the DC electric field.

The incubation time for the onset of flash when the furnace is held at a constant temperature of 780 °C decreases with the magnitude of the applied field, as seen in the inset of Fig. 2c. The temperature of 780 °C was selected because at this temperature the electrical conductivity of the samples reached a measurable value. The decrease suggests that the flash onset is determined by the nucleation of the conducting phase, in this case, carbon [27]. The electric field provides the thermodynamic driving force for the flash event, as to be discussed [22,28].

Since the polymer precursor and the decomposed radicals are insulating, Joule heating causes a drastic sample temperature increase. The sample temperature during the flash event can be much greater than the furnace temperature due to Joule heating. The estimated sample temperature during the flash has been studied in depth and matches quite well with that estimated for blackbody radiation [23,24,29]. The temperature of the samples can be estimated using the following equation [24]:

$$T = T_0\alpha\left[1 + \frac{1000W_v(\text{mW mm}^{-3})}{\sigma T_0^4}\left(\frac{V}{A}(\text{mm})\right)\right]^{1/4} \tag{2}$$

where T is the sample temperature in Kelvin, T_0 is the furnace

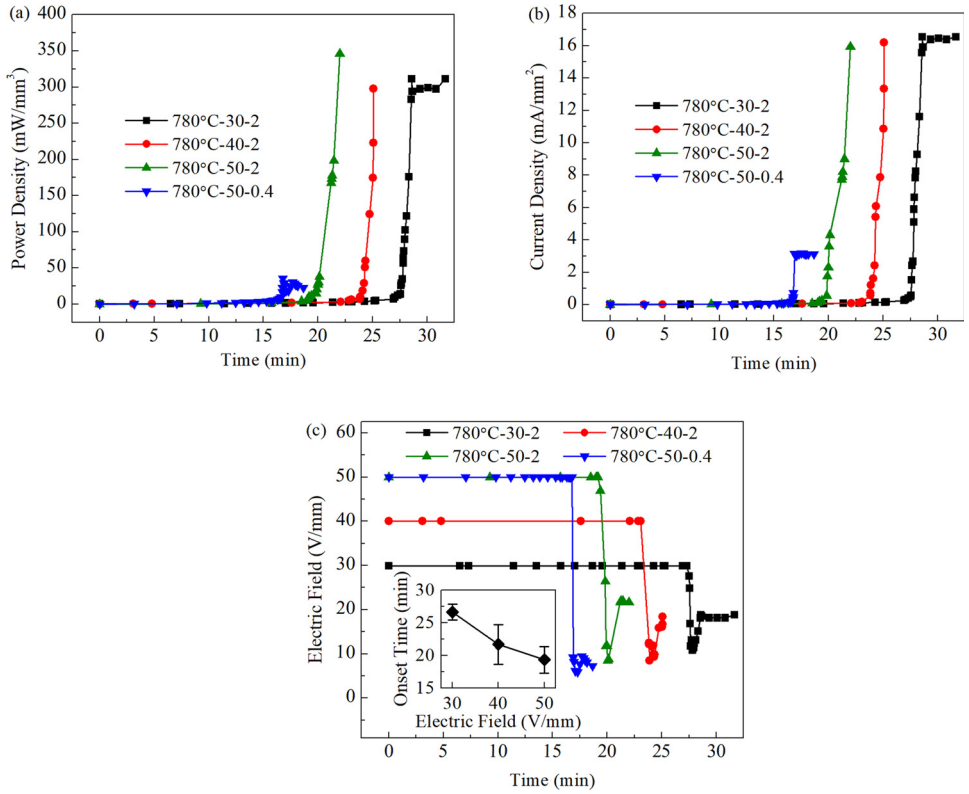

Fig. 2. Changes of (a) power density, (b) current density, and (c) applied electric field during flash pyrolysis.

temperature, σ is the Stefan-Boltzmann constant with a value of 5.67×10^{-8} W m^{-2} K^{-4}, A is the surface area of the sample in mm^2, V is the sample volume in mm^3, α is a correction factor to account for emissivity less than that expected for a perfect blackbody, and W_V is the electrical power dissipated in the sample. Approximating α to be 1, the temperatures of each of the samples in Fig. 2a can be calculated.

The estimated temperature from Eq. (2) is 1304 °C for both the 780 °C-30-2 and 780 °C-40-2 samples (W_V ~300 mW mm^{-3}), 1354 °C for the 780 °C-50-2 sample (W_V ~350 mW mm^{-3}), and 873 °C for the 780 °C-50-0.4 sample (W_V ~30 mW mm^{-3}). The estimated temperatures represent the minimum temperature the samples could obtain because most materials have emissivities lower than a perfect blackbody, which increases α and thus the actual sample temperature [24]. Since these temperatures are very close to the 1300 °C pyrolysis condition without an electric field, the conventional 1300 °C pyrolyzed sample without an electric field will be used as a reference in the following studies.

3.2. Shrinkage and yield

The ceramic yields for the flash pyrolyzed samples are 68.43%–77.86% as shown in Fig. 3. The PSO sample pyrolyzed at 780 °C without any electric field shows the highest ceramic yield of 77.86%. This is well understood as the evaporation of radical species (such as C_2H_2, C_2H_4, or CH_3) is not fully completed at this temperature [30,31]. With the same maximum flash current of 2 A, the ceramic yield decreases with the increasing electric field, even though the lowest yield of 72.32% is still higher than that of the conventional sample pyrolyzed at 1300 °C (68.43%). So one of the advantages of flash pyrolysis is increasing the ceramic yield, by at least 5.7%, which has been an issue for large scale production. A linear fit of the ceramic yield y as a function of the electric field E for the sample without an electric field and the samples with a maximum flash current of 2 A gives the relationship (R^2 = 0.986):

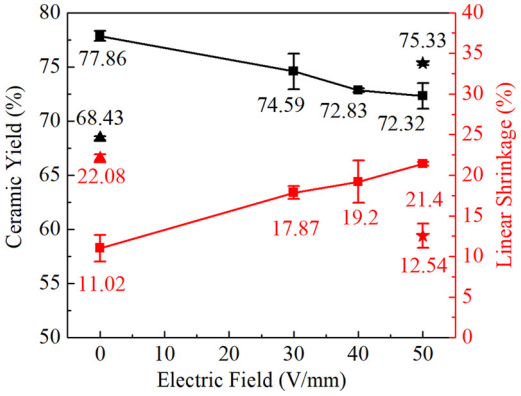

Fig. 3. Shrinkage and ceramic yield of the samples. (■ represents samples pyrolyzed with an electric field and 2 A current limit at 780 °C; ★ represents the 780 °C-50-0.4 sample; ▲ represents the 1300 °C-0-0 sample).

$$y\ (\%) = -0.12E\ \left(\frac{\mathrm{V}}{\mathrm{mm}}\right) + 77.85 \tag{3}$$

Fig. 3 also shows that the ceramic yield for the 780 °C-50-0.4 sample (the ★ symbol, 873 °C calculated internal pyrolysis temperature), 75.33%, is slightly higher than that for the 780 °C-50-2 sample, 72.32% (the ■ symbol, 1354 °C calculated internal pyrolysis temperature), which can be attributed to the difference in Joule heating and thus internal pyrolysis temperature following Eq. (2) as already discussed. Again, the higher ceramic yield is due to the short time scale of the flash event, only several seconds, which does not give adequate time for the gaseous pyrolysis byproducts to completely diffuse out of the sample. By the same token, all the flash pyrolyzed samples have higher ceramic yields than the sample pyrolyzed at 1300 °C, and even higher yields than the samples pyrolyzed at 1100 °C in the absence of the electrical field [32].

The linear shrinkages for the samples after pyrolysis are also shown in Fig. 3, which are 11.02%–22.08%. An important note is that all of the conditions tested resulted in intact bulk samples. However, when a field of 60 V/mm was used, the resulting sample fractured and thus such a high electric field was deemed unsuitable for the study. At the furnace temperature of 780 °C, the linear shrinkage values for the flash pyrolyzed samples are all higher than that without an electric field. This is easy to understand as the sample without the electrical field has barely started any meaningful phase changes. Additionally, for the flash pyrolyzed samples, as the applied electric field increases, the linear shrinkage increases. A curve fitting of the linear shrinkage $\Delta l/l$ as a function of the applied electric field for the sample without an electric field and the samples with a maximum flash current of 2 A gives the relationship ($R^2 = 0.994$):

$$\Delta l/l\,(\%) = 0.21E\left(\frac{\mathrm{V}}{\mathrm{mm}}\right) + 11.17 \tag{4}$$

The 780 °C-50-2 sample has a comparable linear shrinkage to the 1300 °C-0-0 sample without an applied electric field, correlating well with the predicted sample temperature from Eq. (2). However, the furnace temperature is 520 °C lower with the advantage of ~5.7% yield increase. Comparing the two samples with the same electric field but different current limits, the sample with a lower current density, 780 °C-50-0.4, shows much less shrinkage (12.54%) than the 780 °C-50-2 sample (21.4%), due to the lack of microstructure evolution.

3.3. Phase evolution and microstructure

As shown in Fig. 4, all the XRD patterns have an amorphous SiO_2 halo at ~22° [33], and a peak at ~43°; the latter can be assigned to disordered carbon with a turbostratic structure [33–36]. According to the relative height of the 43° peak, the amount of free carbon within the samples is proportional to the electric field intensity. Further, the 26° peak for the 780 °C-50-2 sample, which corresponds to the (002) plane for graphitic materials, is another indication that the carbon formation is increased [36]. This can be explained based on the mechanism that the electric field provides an additional nucleation driving force for the conductive carbon phase (see below) and more importantly carbon ordering through electromigration. For the flash-pyrolyzed samples, the diffraction peaks at 35.5°, 41.4°, 60°, and 72° appear, corresponding to the (111), (200), (220), and (311) crystallographic planes of β-SiC [37]. The formation of the SiO_2, C, and SiC phases occurs through the phase separation of the SiOC matrix (~1300 °C), and SiC can further form through the carbothermal reduction of SiO_2 (> 1300 °C) [3,6]:

$$2SiOC \rightarrow SiO_2 + SiC + C \tag{5}$$

$$SiO_2 + 3C \rightarrow SiC + 2CO \tag{6}$$

Fig. 4b clearly shows that without the electrical field, there is no SiC formation. In the presence of the electric field, the SiO_2 content consistently decreases while the SiC content consistently increases with the electric field increase. The carbon content first increases when the electric field increases from 30 V mm^{-1} to 40 V mm^{-1} but then decreases at 50 V mm^{-1}. This means that significant phase separation in the flash-pyrolyzed samples takes place at a furnace temperature of 780 °C, which is more than 500 °C lower than that for traditional pyrolysis, 1300 °C. Furthermore, the amount of β-SiC in the flash-pyrolyzed samples is proportional to the applied electric field, proving that the SiC crystallization is facilitated by the increased carbon content, meaning that increased carbon accelerates the onset of the SiC crystallization in SiOC [10].

The driving force for nucleation arises from the polarization energy of carbon, and the polarization energy per unit volume, ΔG_V, is given by [28]:

$$\Delta G_V = \frac{1}{2}\varepsilon_o\varepsilon_E E^2 + \Delta G_{V,0} \tag{7}$$

where ε_o is the permittivity of free space, 8.85×10^{-12} $A^2\,s^4\,kg^{-1}\,m^{-3}$, ε_E is the dielectric constant of the carbon nuclei, E is the applied electric field, and $\Delta G_{V,0}$ is the energy of formation per unit volume without an electric field. The growth of the embryo is opposed by the energy of the interface it forms with the parent lattice, γ_E. The total free energy of the embryo, relative to the zero-field state, is then given by

$$\Delta G = -\frac{4}{3}\pi r^3\Delta G_V + 4\pi r^2\gamma_E \tag{8}$$

When the driving force is higher than the opposing surface energy, the nucleation initiates. Taking the derivative of ΔG with respect to r and setting it equal to 0 give the critical radius for nucleation, r*, and plugging r* back into the Eq. (8) gives the energy barrier that needs to be overcome for nucleation, ΔG*:

$$r^* = \frac{4\gamma_E}{\varepsilon_o\varepsilon_E E^2 + 2\Delta G_{V0}} \tag{9}$$

$$\Delta G^* = \frac{64\pi\gamma_E^3}{3[\varepsilon_o\varepsilon_E E^2 + 2\Delta G_{V0}]^2} \tag{10}$$

The value of ΔG_{V0} can be approximated as the enthalpy of formation of turbostratic carbon [38], 1.7×10^9 J m^{-3}, ε_E is estimated to be 10 [39], γ_E is estimated as 1 J m^{-2} [28]. The enthalpy of formation is converted from molar enthalpy (20,800 J mol^{-1}) [38] through multiplying by the density of turbostratic carbon (~2000 kg m^{-3}) [40,41] and dividing by the molar mass (24×10^{-3} kg mol^{-1} assuming a single graphene-like structure). The critical radius (Eq. (9)) and the energy barrier (Eq. (10)) are 1.2 nm and 5.6×10^{-18} J, respectively. With and without an applied electric field, these values are almost the same since the electric field contribution in Eqs. (7)–(10) is 10 orders of magnitude smaller than the ΔG_{V0} term. With a field of 50 V mm^{-1}, the critical

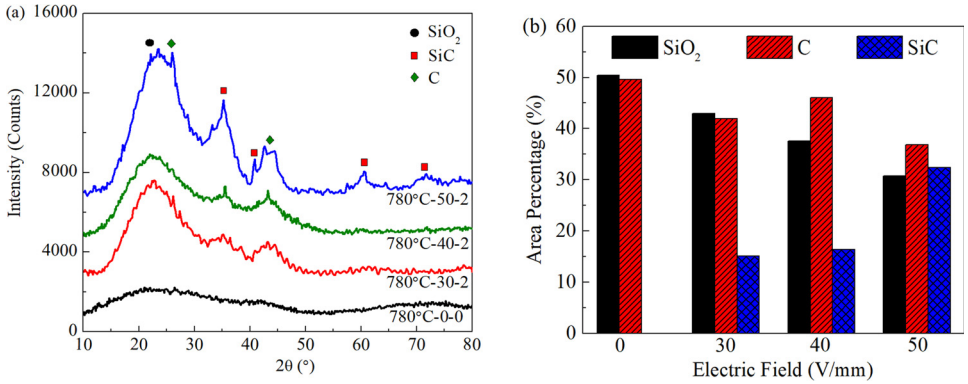

Fig. 4. (a) XRD patterns for the samples pyrolyzed with different electric fields at 780 °C, and (b) area percentages of the SiO_2 (21.9°), SiC (35.6°, 60°, 72°), and C (26°, 43°) phases.

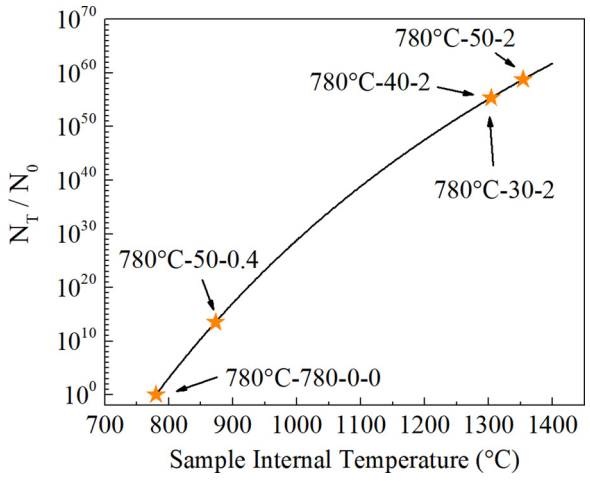

Fig. 5. Effect of Joule heating on nuclei concentration at 780 °C furnace temperature. The ★ symbols represent the experimental conditions.

nucleus is reduced by only 7×10^{-20} m compared to that without an electric field, and the energy barrier is reduced by 7×10^{-28} J. Thus, the ΔG_{V0} term more significantly impacts the critical nuclei size and energy than the $\varepsilon_o \varepsilon_E E_j^2$ term, resulting in similar carbon nuclei sizes in both cases.

The concentration of stable carbon nuclei relative to the carbon concentration in the bulk SiOC, N, is related to ΔG^* as [27,28]:

$$N \propto \exp\left(-\frac{\Delta G^*}{kT}\right) \tag{11}$$

where k is the Boltzmann constant, 1.38×10^{-23} J K^{-1}, and the temperature T is the sample temperature. From Eq. (11), the nuclei concentration at 780 °C under an electric field relative to that without an electric field, N_T/N_0, is plotted as a function of the sample internal temperature in Fig. 5. As the sample temperature rises above the furnace temperature of 780 °C, the nucleation rate increases exponentially, reaching a stable nuclei concentration of $\sim 10^{59}$ times that of the zero field for the 780 °C-50-2 sample. Thus, while the critical nuclei size and energy are not significantly affected by the applied electric field, the stable nuclei concentration is dramatically enhanced by Joule heating during the flash event, leading to more carbon within the samples with the applied electric field (Fig. 4).

In order to understand the influence of the current density, PSO was pyrolyzed with different current limits. The XRD patterns are shown in Fig. 6. No β-SiC diffraction peaks are observed for the sample with a lower current limit of 0.4 A. This is because the lower current density only allows for the Joule heating to ~873 °C, which is not high enough to facilitate the SiC formation compared to the ~1354 °C internal temperature attained by the 780 °C-50-2 sample. However, the electric field is sufficient for carbon domain formation as expressed by Eqs. (7)–(11), demonstrated by the hump at 43° on the XRD pattern. Further, the XRD pattern for the 780 °C-50-2 sample closely resembles that of the 1300 °C-0-0 sample, confirming that the 780 °C-50-2 sample has experienced Joule heating to the approximate temperature predicted by Eq. (2). Therefore, the electric field accelerates the phase separation and carbon formation.

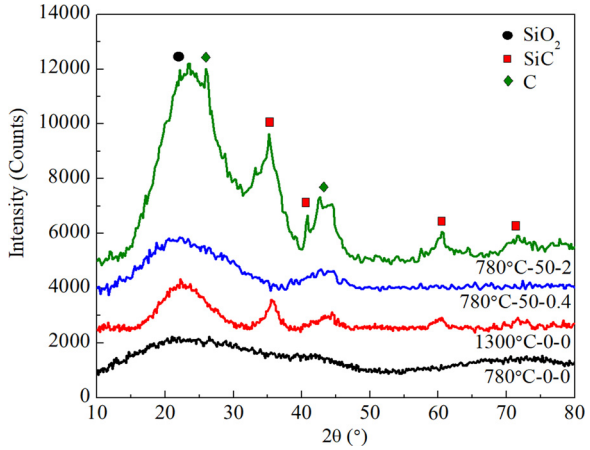

Fig. 6. XRD patterns for the samples pyrolyzed at 780 °C and 1300 °C, either without an electric field or with an electric field of 50 V mm^{-1}.

The carbon phase evolution can be further explained as follows. First, the electric field acts as the driving force for the carbon nuclei formation during the incubation period (Eqs. (7)–(11). Therefore, more carbon is obtained with a higher electric field. Then, Joule heating (Eq. (2)) increases the sample temperature, creating conditions for further C formation as well as SiC formation through SiOC phase separation (Eq. (5)) or carbothermal reduction of SiO_2 (Eq. (6)).

In the Raman spectra of the SiOC samples, there are two significant bands present at 1340 and 1590 cm^{-1}, corresponding to the D and G bands of carbon (Fig. 7). The D-band is associated with the vibration mode of defective graphene layers, and the G-mode comes from the in-plane bond stretching of sp^2 carbon atoms [42–44]. As shown in Fig. 7a, all of the pyrolyzed samples display the D and G bands, and the G peak for all the samples is at ~1590 cm^{-1}, both being typical features of a disordered sp^2-hybridized segregated carbon phase [44].

In addition to the D and G peaks, there is also an additional peak at ~1500 cm^{-1} that corresponds to amorphous carbon (a-C) [45,46]. The D, G, and a-C peaks are deconvoluted (Fig. 7b), and their relative integrated intensities (I(D), I(G), and I(a-C), respectively) are given in Table 1. The relative intensity of the D peak is largely unaffected for all of the samples, indicating that the electric field does not significantly influence the defect concentration within the crystalline carbon phase. For the samples pyrolyzed at 780 °C with the 2 A current limit, the relative intensity of the a-C peak decreases with increasing electric field while the G peak intensity increases; this means an increase in the graphitization of the samples, which is an ordering of the graphitic phase from amorphous carbon into nanocrystalline carbon [45]. The increased graphitization is also seen for the 1300 °C-0-0 sample, which has a lower I(a-C) and higher I(G) compared to the 780 °C-0-0 sample. However, the 1300 °C-0-0 sample still has a higher I(a-C) and lower I(G) compared to the 780 °C-40-2 and 780 °C-50-2 samples, confirming that the applied electric field can induce more effective ordering of the carbon phase compared to heating the samples without an electric field.

The ordering of carbon under an electric field has also been shown for other carbonaceous materials [26,47,48]. The mechanism for this ordering is through electromigration, the transfer of momentum from drifting electrons to defects within the carbon phase. The effective force that the electrons impart on the defects, F_{wind}, is given by [26,49]:

$$F_{wind} = -e \cdot Z^* \cdot E \tag{12}$$

where Z^* is the effective valence of the material and e is the elemental charge. The momentum transfer increases the mobility of the defects, which is further increased by Joule heating, allowing for the defects to diffuse out of the carbon matrix and increasing the ordering of the carbon phase. [26] The flux of defects due to this momentum transfer, J, is [26,49,50]:

$$J = \frac{N_v D e Z^* E}{kT} \tag{13}$$

where N_v is the vacancy concentration and D is the diffusivity, both of which further rely on the temperature through an Arrhenius relationship [49,51]. Thus, the flux of the defects is given as:

$$J = N_o D_o Z^* \left(\frac{eE}{kT}\right) \cdot \exp\left(\frac{-E_{f,v}}{kT}\right) \cdot \exp\left(\frac{-E_a}{kT}\right) \tag{14}$$

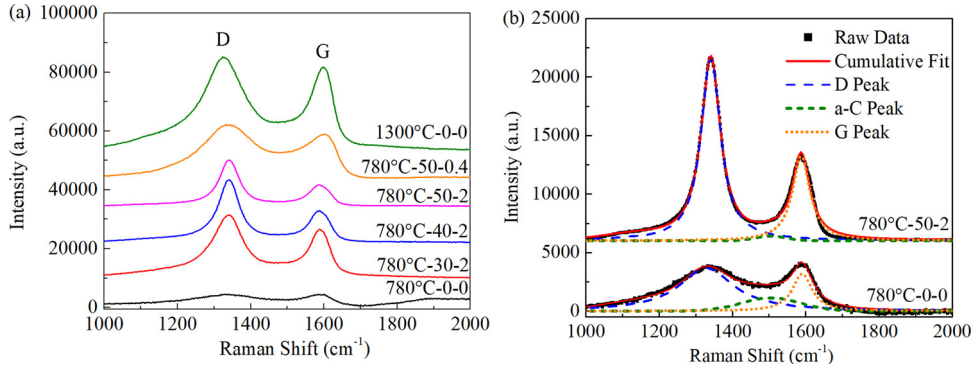

Fig. 7. (a) Raman spectra of different samples, and (b) examples of the deconvolution of the D, G, and a-C peaks for the 780 °C-0-0 and 780 °C-50-2 samples.

Table 1
Results of Raman fitting for the studied samples.

Sample	I(D) (%)	I(G) (%)	I(a-C) (%)	L_a (nm)
780 °C-0-0	66	20	14	1.4
780 °C-30-2	67	28	5	1.5
780 °C-40-2	69	28	3	1.9
780 °C-50-2	69	29	2	2.0
780 °C-50-0.4	68	19	13	1.6
1300 °C-0-0	68	27	5	1.4

where N_o is the number of atomic sites per volume, D_o is the temperature independent diffusion preexponential, $E_{f,v}$ is the formation energy of vacancies, and E_a is the activation energy for vacancy diffusion [49]. Eq. (14) can be rewritten as

$$J = C \cdot J(E, T) \tag{15}$$

where C represents the independent material properties $N_o D_o Z^*$ and $J(E,T)$ represents the terms affected by the electric field and the sample temperature, $\left(\frac{eE}{kT}\right)\cdot\exp\left(\frac{-E_{f,v}}{kT}\right)\cdot\exp\left(\frac{-E_a}{kT}\right)$. Using the values for single vacancy formation and diffusion in graphene, the formation energy for vacancies is approximated as 1.2×10^{-18} J [52,53], and the activation energy for vacancy diffusion is approximated as 1.9×10^{-19} J [52]. Plots of $J(E,T)$ as a function of electric field and sample temperature are shown in Fig. 8. The increased sample temperature from Joule heating has a much greater influence on the defect flux, and thus graphitization, than the electric field. The defect flux for the 780 °C-50-0.4 sample is significantly less than that for the 780 °C-30-2, 780 °C-40-2, and 780 °C-50-2 samples due to the lower Joule heating. Fig. 8 matches well with the experimental Raman results, in which the 780 °C-50-0.4 sample displays similar I(G) and I(a-C) values as the 780 °C-0-0 sample, indicating a disordered carbon phase, while the 780 °C-30-2, 780 °C-40-2, and 780 °C-50-2 samples have much more ordered graphitic structures. Thus, the main driving force for the graphitization of the carbon within the SiOC sample is synergistic Joule heating and electromigration; without significant Joule heating, the carbon phase remains in its original disordered state.

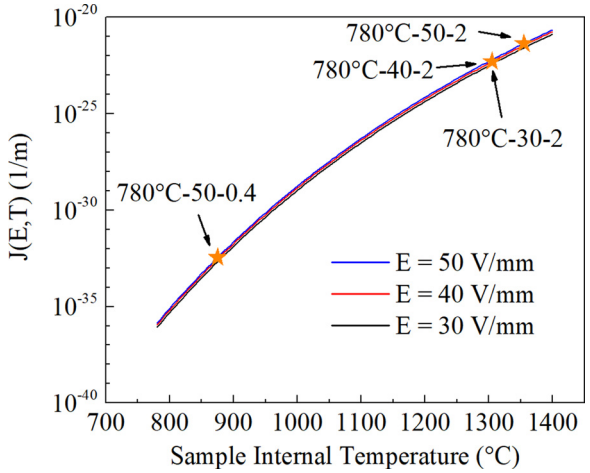

Fig. 8. Plots of $J(E,T)$ for applied electric fields of 30 V mm^{-1}, 40 V mm^{-1}, and 50 V mm^{-1}. The ★ symbols represent the experimental conditions.

The carbon crystallite size, L_a, can be estimated using the relation [44,54]:

$$\left(\frac{I_D}{I_G}\right) = C(\lambda) L_a^2 \tag{16}$$

where $C(\lambda)$ is 0.0055 Å^{-2} with a laser wavelength of 514 nm from the Raman spectroscopy and I_D and I_G are the intensities of the D and G peaks, respectively, after deconvolution. The results of applying Eq. (16) for all of the samples are shown in Table 1. At 780 °C, L_a increases from ~1.4 nm for the sample with no electric field to ~2.0 nm for the 780 °C-50-2 sample. Similarly, the 1300 °C-0-0 sample also has a L_a value of ~1.4 nm, and the 780 °C-50-0.4 sample has a L_a value of ~1.6 nm. Thus, under the electric field, the thermal condition inside the flash pyrolyzed sample can activate the carbon phase growth at more than 500 °C lower temperature than that without an electric field. These carbon crystallite sizes are also only slightly greater than the carbon nuclei size of 1.2 nm calculated from Eq. (9). This means that crystal growth in the studied SiOC samples is very limited, which is consistent with the extremely short burst of heating during flash.

The microstructures of the 780 °C-0-0, 780 °C-50-0.4, and 780 °C-50-2 samples are shown in Fig. 9. Without an electric field (Fig. 9a), the SiOC is completely amorphous, with no crystalline phase. There are several small lamellar regions with darker contrast and a separation distance of ~0.35 nm, which can be attributed to "basic structural units" (BSU) of carbon [55,56]. The lateral sizes for the BSUs are ~1–2 nm, agreeing with the Raman results and the calculated carbon nuclei size (Eq. (9)). For the 780 °C-50-0.4 sample (Fig. 9b), the application of an electric field without significant Joule heating does not cause a significant change in the microstructure, which is still composed of a primarily amorphous matrix with several carbon BSUs dispersed throughout, even though the dark contrast regions are more visible and larger than ~1 nm. Further, along the edges of the sample, the BSUs are longer and directionally aligned. With both high electric field and significant Joule heating (Fig. 9c), the 780 °C-50-2 sample shows significantly larger and more well-ordered carbon regions, especially near the edges of the sample, and a crystalline SiC phase. The TEM results match well with the XRD patterns in Fig. 6 and the Raman spectra is Fig. 7a in that the 780-50-2 sample has both SiC and a much more ordered carbon phase than both the 780-0-0 and 780-50-0.4 samples.

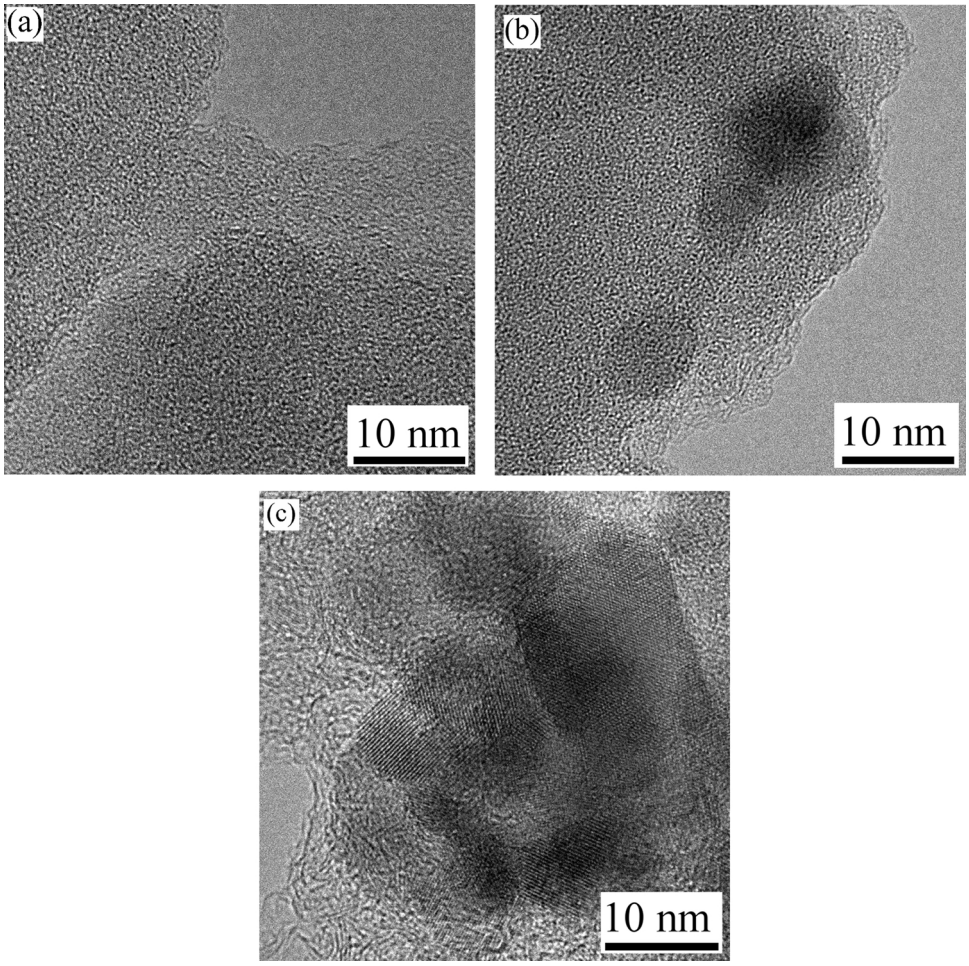

Fig. 9. TEM microstructures of the (a 780 °C-0-0, (b 780 °C-50-0.4, and (c 780 °C-50-2 samples.

3.4. Electrical conductivity

The electrical conductivity of SiOC ceramics is heavily dependent on the carbon content within the ceramics [9–11,57]. Room temperature electric conductivities for all of the samples are shown in Fig. 10. Considering just traditional heating without an electric field, the conductivity increases greatly from $\sim 10^{-9}$ S cm^{-1} to $\sim 10^{-1}$ S cm^{-1} as the pyrolysis temperature increases from 780 °C to 1300 °C. With the application of the electric field at 780 °C, the conductivity increases 6 orders of magnitude from the 780 °C-0-0 sample (10^{-9} S cm^{-1}) to the 780 °C-30-2 sample (2×10^{-3} S cm^{-1}). Consistent with Fig. 4b, the combined electric field and Joule heating facilitate carbon precipitation from the SiOC matrix as already discussed. With even higher electric fields, however, the conductivity decreases from $\sim 10^{-3}$ S cm^{-1} for the 780 °C-30-2 sample to $\sim 10^{-5}$ S cm^{-1} for the 780 °C-40-2 sample and $\sim 10^{-7}$ S cm^{-1} for the 780 °C-50-2 sample. This is because with higher electric field and Joule heating, increased SiC formation decreases the carbon content and disrupts the conductive percolating network. For the 780 °C-50-0.4 sample, the electrical conductivity is significantly greater than that for the 780 °C-0-0 sample. This again reflects the important role of carbon availability for the electrical conductivity.

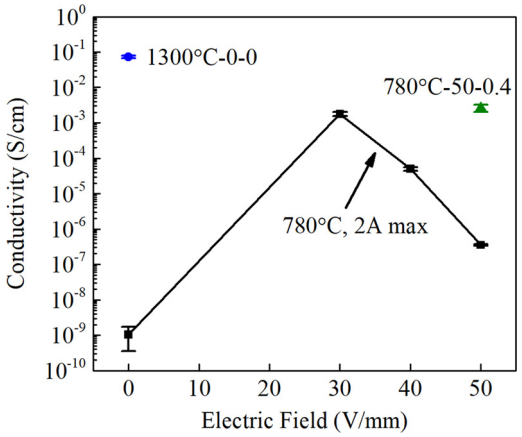

Fig. 10. Electrical conductivities of the samples pyrolyzed at various conditions.

Comparing the Raman spectroscopy results in Table 1 and the electrical conductivity results in Fig. 10, important conclusions about the timing of events occurring during flash pyrolysis can be made. While both the 780 °C-0-0 and 780-50-0.4 samples contain similar disordered carbon phases, the conductivity of the 780 °C-50-0.4 sample is six orders of magnitude greater than that of the 780 °C-0-0 sample, indicating that the carbon content of the 780 °C-50-0.4 sample is increased while remaining in a disordered state. The electric field leads to a higher carbon concentration (Eqs. (7)–(11)) even though not enough Joule heating is provided to cause further ordering. On the other hand, the 780 °C-50-2 sample has the most ordered graphitic phase but an electrical conductivity four orders of magnitude less than the 780 °C-50-0.4 sample. This is because the high applied electric field in combination with Joule heating encourage consumption of the carbon phase to form SiC, lowering the total carbon content and thus the electrical conductivity, while also providing the thermal energy to graphitize the

remaining carbon through electromigration.

4. Conclusions

Flash pyrolysis was employed for the first time to produce polymer-derived SiOC ceramics. The effects of both the applied electric field and Joule heating on the ceramic yield, linear shrinkage, and phase evolution were studied. With the application of an electric field, the samples experience Joule heating that results in similar ceramic yield and linear shrinkage values at > 500 °C lower pyrolysis temperatures, a remarkable result in light of the high temperature needed for such a process. The fundamental driving force for the SiOC phase evolution is rooted in the additional driving force for new phase nucleation due to the electrical field. The applied electric field, simultaneous Joule heating, and electromigration are distinct events leading to carbon nucleation and ordering as well as SiC formation. With both a high electric field and significant Joule heating, the formation of SiC is promoted due to the availability of carbon and the amorphous nature of the C- and Si-containing species present. Flash pyrolysis offers a low-temperature and highly efficient process for polymer derived SiOC fabrication.

Conflicts of interest

There are no conflicts to declare.

Data availability

The raw data required to reproduce these findings are available to download from https://data.lib.vt.edu/.

Acknowledgement

We acknowledge the financial support from National Science Foundation under grant number CMMI-1634325.

References

[1] E. Ionescu, H.J. Kleebe, R. Riedel, Silicon-containing polymer-derived ceramic nanocomposites (PDC-NCs): preparative approaches and properties, Chem. Soc. Rev. 41 (2012) 5032–5052.
[2] P. Colombo, G. Mera, R. Riedel, G.D. Soraru, Polymer-derived ceramics: 40 years of research and innovation in advanced ceramics, J. Am. Ceram. Soc. 93 (2010) 1805–1837.
[3] K. Lu, Porous and high surface area silicon oxycarbide-based materials-a review, Mater. Sci. Eng. R Rep. 97 (2015) 23–49.
[4] L.Q. Duan, Q.S. Ma, Effect of pyrolysis temperature on the pore structure evolution of polysiloxane-derived ceramics, Ceram. Int. 38 (2012) 2667–2671.
[5] H. Brequel, J. Parmentier, G.D. Soraru, L. Schiffini, S. Enzo, Study of the phase separation in amorphous silicon oxycarbide glasses under heat treatment, Nanostruct. Mater. 11 (1999) 721–731.
[6] A. Saha, R. Raj, Crystallization maps for SiCO amorphous ceramics, J. Am. Ceram. Soc. 90 (2007) 578–583.
[7] A. Saha, R. Raj, D.L. Williamson, A model for the nanodomains in polymer-derived SiCO, J. Am. Ceram. Soc. 89 (2006) 2188–2195.
[8] H. Brequel, J. Parmentier, S. Walter, R. Badheka, G. Trimmel, S. Masse, J. Latournerie, P. Dempsey, C. Turquat, A. Desmartin-Chomel, L. Le Neindre-Prum, U.A. Jayasooriya, D. Hourlier, H.J. Kleebe, G.D. Soraru, S. Enzo, F. Babonneau, Systematic structural characterization of the high-temperature behavior of nearly stoichiometric silicon oxycarbide glasses, Chem. Mater. 16 (2004) 2585–2598.
[9] K. Lu, D. Erb, M. Liu, Thermal stability and electrical conductivity of carbon-enriched silicon oxycarbide, J. Mater. Chem. C 4 (2016) 1829–1837.
[10] K. Lu, D. Erb, M.Y. Liu, Phase transformation, oxidation stability, and electrical conductivity of TiO_2-polysiloxane derived ceramics, J. Mater. Sci. 51 (2016) 10166–10177.
[11] J. Cordelair, P. Greil, Electrical conductivity measurements as a microprobe for structure transitions in polysiloxane derived Si-O-C ceramics, J. Eur. Ceram. Soc. 20 (2000) 1947–1957.
[12] G.A. Danko, R. Silberglitt, P. Colombo, E. Pippel, J. Woltersdorf, Comparison of microwave hybrid and conventional heating of preceramic polymers to form silicon carbide and silicon oxycarbide ceramics, J. Am. Ceram. Soc. 83 (2000) 1617–1625.
[13] M.A. Mazo, A. Tamayo, A.C. Caballero, J. Rubio, Electrical and thermal response of silicon oxycarbide materials obtained by spark plasma sintering, J. Eur. Ceram. Soc. 37 (2017) 2011–2020.
[14] A. Tamayo, M.A. Mazo, F. Rubio, J. Rubio, Structure properties relationship in silicon oxycarbide glasses obtained by spark plasma sintering, Ceram. Int. 40 (2014) 11351–11358.
[15] M. Esfehanian, R. Oberacker, T. Fett, M.J. Hoffmann, Development of dense filler-free polymer-derived SiOC ceramics by field-assisted sintering, J. Am. Ceram. Soc. 91 (2008) 3803–3805.
[16] K.G. Schell, E.C. Bucharsky, R. Oberacker, M.J. Hoffmann, Determination of sub-critical crack growth parameters in polymer-derived SiOC ceramics by biaxial bending tests in water environment, J. Am. Ceram. Soc. 93 (2010) 1540–1543.
[17] E. Reitz, K.G. Schell, E.C. Bucharsky, R. Oberacker, M.J. Hoffmann, Precursor derived SiOC/$MoSi_2$-composites for diesel glow plugs: preparation and high temperature properties, J. Ceram. Soc. Jpn. 124 (2016) 1017–1022.
[18] P. Miranzo, C. Ramírez, B. Román-Manso, L. Garzón, H.R. Gutiérrez, M. Terrones, C. Ocal, M.I. Osendi, M. Belmonte, In situ processing of electrically conducting graphene/SiC nanocomposites, J. Eur. Ceram. Soc. 33 (2013) 1665–1674.
[19] M. Cologna, B. Rashkova, R. Raj, Flash sintering of nanograin zirconia in < 5 s at 850 degrees C, J. Am. Ceram. Soc. 93 (2010) 3556–3559.
[20] M. Cologna, J.S.C. Francis, R. Raj, Field assisted and flash sintering of alumina and its relationship to conductivity and MgO-doping, J. Eur. Ceram. Soc. 31 (2011) 2827–2837.
[21] M. Cologna, A.L.G. Prette, R. Raj, Flash-sintering of cubic yttria-stabilized zirconia at 750 °C for possible use in SOFC manufacturing, J. Am. Ceram. Soc. 94 (2011) 316–319.
[22] J.S.C. Francis, R. Raj, Influence of the field and the current limit on flash sintering at isothermal furnace temperatures, J. Am. Ceram. Soc. 96 (2013) 2754–2758.
[23] J.S.C. Francis, R. Raj, Flash-sinterforging of nanograin zirconia: field assisted sintering and superplasticity, J. Am. Ceram. Soc. 95 (2012) 138–146.
[24] R. Raj, Joule heating during flash-sintering, J. Eur. Ceram. Soc. 32 (2012) 2293–2301.
[25] R. Raj, Analysis of the power density at the onset of flash sintering, J. Am. Ceram. Soc. 99 (2016) 3226–3232.
[26] B. Wang, D.E. Wolfe, M. Terrones, M.A. Haque, S. Ganguly, A.K. Roy, Electro-graphitization and exfoliation of graphene on carbon nanofibers, Carbon 117 (2017) 201–207.
[27] J.C. Fisher, J.H. Hollomon, D. Turnbull, Nucleation, J. Appl. Phys. 19 (1948) 775–784.
[28] K.S. Naik, V.M. Sglavo, R. Raj, Flash sintering as a nucleation phenomenon and a model thereof, J. Eur. Ceram. Soc. 34 (2014) 4063–4067.
[29] H. Yoshida, Y. Sakka, T. Yamamoto, J.M. Lebrun, R. Raj, Densification behaviour and microstructural development in undoped yttria prepared by flash-sintering, J. Eur. Ceram. Soc. 34 (2014) 991–1000.
[30] D. Hourlier, S. Venkatachalam, M.R. Ammar, Y. Blum, Pyrolytic conversion of organopolysiloxanes, J. Anal. Appl. Pyrolysis 123 (2017) 296–306.
[31] X. Wang, J. Wu, Y. Li, C. Zhou, C. Xu, Pyrolysis kinetics and pathway of polysiloxane conversion to an amorphous SiOC ceramic, J. Therm. Anal. Calorim. 115 (2014) 55–62.
[32] J.K. Li, K. Lu, T.S. Lin, F.Y. Shen, Preparation of micro-/mesoporous SiOC bulk ceramics, J. Am. Ceram. Soc. 98 (2015) 1753–1761.
[33] R. Peña-Alonso, G.D. Sorarù, R. Raj, Preparation of ultrathin-walled carbon-based nanoporous structures by etching pseudo-amorphous silicon oxycarbide ceramics, J. Am. Ceram. Soc. 89 (2006) 2473–2480.
[34] A.M. Wilson, G. Zank, K. Eguchi, W. Xing, B. Yates, J.R. Dahn, Pore creation in silicon oxycarbides by rinsing in dilute hydrofluoric acid, Chem. Mater. 9 (1997) 2139–2144.
[35] R. Pena-Alonso, G. Mariotto, C. Gervais, F. Babonneau, G.D. Soraru, New insights on the high-temperature nanostructure evolution of SiOC and B-doped SiBOC polymer-derived glasses, Chem. Mater. 19 (2007) 5694–5702.
[36] Z.Q. Li, C.J. Lu, Z.P. Xia, Y. Zhou, Z. Luo, X-ray diffraction patterns of graphite and turbostratic carbon, Carbon 45 (2007) 1686–1695.
[37] D. Erb, K. Lu, Additive and pyrolysis atmosphere effects on polysiloxane-derived porous SiOC ceramics, J. Eur. Ceram. Soc. 37 (2017) 4547–4557.
[38] A.H. Tavakoli, M.M. Armentrout, M. Narisawa, S. Sen, A. Navrotsky, White Si-O-C ceramic: structure and thermodynamic stability, J. Am. Ceram. Soc. 98 (2015) 242–246.
[39] T. Kim, J. Lee, K.-H. Lee, Full graphitization of amorphous carbon by microwave heating, RSC Adv. 6 (2016) 24667–24674.
[40] C. Pradere, J.C. Batsale, J.M. Goyhénèche, R. Pailler, S. Dilhaire, Thermal properties of carbon fibers at very high temperature, Carbon 47 (2009) 737–743.
[41] N.E.S. Sazali, M. Deraman, R. Omar, M.A.R. Othman, M. Suleman, S.A. Shamsudin, N.S.M. Tajuddin, M.F.Y.M. Hanappi, E. Hamdan, N.S.M. Nor, N.H. Basri, Preparation and structural characterization of turbostratic-carbon/graphene derived from amylose film, AIP Conf. Proc. 1784 (2016) 040009.
[42] M. Graczyk-Zajac, L. Toma, C. Fasel, R. Riedel, Carbon-rich SiOC anodes for lithium-ion batteries: part I. Influence of material UV-pre-treatment on high power properties, Solid State Ionics 225 (2012) 522–526.
[43] L.G. Cançado, K. Takai, T. Enoki, M. Endo, Y.A. Kim, H. Mizusaki, A. Jorio, L.N. Coelho, R. Magalhães-Paniago, M.A. Pimenta, T. F, K.J. L, General equation for the determination of the crystallite size La of nanographite by Raman spectroscopy, Appl. Phys. Lett. 88 (2006) 163106.
[44] A.C. Ferrari, J. Robertson, Interpretation of Raman spectra of disordered and amorphous carbon, Phys. Rev. B 61 (2000) 14095–14107.
[45] F. Roth, P. Waleska, C. Hess, E. Ionescu, N. Nicoloso, UV Raman spectroscopy of segregated carbon in silicon oxycarbides, J. Ceram. Soc. Jpn. 124 (2016) 1042–1045.
[46] N. Larouche, B.L. Stansfield, Classifying nanostructured carbons using graphitic indices derived from Raman spectra, Carbon 48 (2010) 620–629.

[47] X. Jia, M. Hofmann, V. Meunier, B.G. Sumpter, J. Campos-Delgado, J.M. Romo-Herrera, H. Son, Y.-P. Hsieh, A. Reina, J. Kong, M. Terrones, M.S. Dresselhaus, Controlled formation of sharp zigzag and armchair edges in graphitic nanoribbons, Science 323 (2009) 1701–1705.
[48] Y. Yu, S. Luo, L. Sun, Y. Wu, K. Jiang, Q. Li, J. Wang, S. Fan, Ultra-stretchable conductors based on buckled super-aligned carbon nanotube films, Nanoscale 7 (2015) 10178–10185.
[49] R.L. de Orio, H. Ceric, S. Selberherr, Physically based models of electromigration: from Black's equation to modern TCAD models, Microelectron. Reliab. 50 (2010) 775–789.
[50] Y.F. Huang, Z.X. Deng, W.L. Wang, C.L. Liang, J.C. She, S.Z. Deng, N.S. Xu, Field-induced crystalline-to-amorphous phase transformation on the Si nano-apex and the achieving of highly reliable Si nano-cathodes, Sci. Rep. 5 (2015).
[51] H. Bracht, A. Chroneos, The vacancy in silicon: a critical evaluation of experimental and theoretical results, J. Appl. Phys. 104 (2008) 076108.
[52] J.D. Wadey, A. Markevich, A. Robertson, J. Warner, A. Kirkland, E. Besley, Mechanisms of monovacancy diffusion in graphene, Chem. Phys. Lett. 648 (2016) 161–165.
[53] W.C. Tian, W.H. Li, W.B. Yu, X.H. Liu, A review on lattice defects in graphene: types, generation, effects and regulation, Micromachines 8 (2017) 163.
[54] F. Roth, C. Schmerbauch, E. Ionescu, N. Nicoloso, O. Guillon, R. Riedel, High-temperature piezoresistive C/SiOC sensors, J. Sens. Sens. Syst. 4 (2015) 133–136.
[55] C. Turquat, H.J. Kleebe, G. Gregori, S. Walter, G.D. Soraru, Transmission electron microscopy and electron energy-loss spectroscopy study of nonstoichiometric silicon-carbon-oxygen glasses, J. Am. Ceram. Soc. 84 (2001) 2189–2196.
[56] H.J. Kleebe, C. Turquat, G.D. Soraru, Phase separation in an SiCO glass studied by transmission electron microscopy and electron energy-loss spectroscopy, J. Am. Ceram. Soc. 84 (2001) 1073–1080.
[57] K.J. Kim, J.H. Eom, Y.W. Kim, W.S. Seo, Electrical conductivity of dense, bulk silicon-oxycarbide ceramics, J. Eur. Ceram. Soc. 35 (2015) 1355–1360.